Journal of Colloid and Interface Science 437 (2015) 252–258

Contents lists available at ScienceDirect

Journal of Colloid and Interface Science

www.elsevier.com/locate/jcis

# Ethanol chemiresistor with enhanced discriminative ability from acetone based on Sr-doped $SnO_2$ nanofibers

Ziqiao Jiang [a], Tingting Jiang [a,b], Jinfeng Wang [c], Zhaojie Wang [a], Xiuru Xu [a], Zongxin Wang [a], Rui Zhao [a], Zhenyu Li [a,c,*], Ce Wang [a,*]

[a] Alan G. MacDiarmid Institute, Jilin University, Changchun 130012, PR China
[b] Department of Catalysis Science and Engineering, School of Chemical Engineering and Technology, Harbin Institute of Technology, Harbin 150001, PR China
[c] Australian Future Fibres Research & Innovation Centre, Institute for Frontier Materials, Deakin University, Geelong, Victoria 3217, Australia

ARTICLE INFO

*Article history:*
Received 30 June 2014
Accepted 22 September 2014
Available online 30 September 2014

*Keywords:*
Sr-functionalized $SnO_2$
Ethanol sensor
Electrospinning
Selectivity
Rapid
Sensitive

ABSTRACT

We demonstrated a new metal oxides based chemiresistor (MOC), which exhibits fast response/recovery behavior, large sensitivity, and good selectivity to ethanol, enabled by Sr-doped $SnO_2$ nanofibers via simple electrospinning and followed by calcination. Transmission electron microscopy (TEM), scanning electron microscopy (SEM), X-ray diffraction (XRD), and X-ray photoelectron spectra (XPS) were carefully used to characterize their morphology, structure, and composition. The ethanol sensing performances based on Sr-doped $SnO_2$ nanofibers were investigated. Comparing with the pristine $SnO_2$ nanofibers, enhanced ethanol sensing performances (more rapid response/recovery behavior and larger response values) have been achieved owing to the basic $SnO_2$ surface caused by Sr-doping, whereas the acetone sensing performances have been weakened. Thus, good discriminative ability to ethanol from acetone has been realized. Additionally, Sr-doped $SnO_2$ nanofibers also exhibit good selectivity.



## 1. Introduction

Metal oxides based chemiresistors (MOCs) have been widely investigated for decades driven by their practical applications in air quality control, environmental monitoring, healthcare, traffic safety, etc. [1–4]. To improve the gas sensing performances, a general route is to construct one-dimensional (1D) nano-scaled metal oxides as gas-sensing elements. 1D nanostructures offer large surface-to-volume ratios and unique dimensional electrical transport, which can provide more active sites on the surface and effectively reduce the electric carriers scattering compared to zero-dimensional nanostructures [5–10]. Among those 1D metal oxide nanostructures, electrospun 1D metal oxides have been demonstrated to be excellent candidates for high-efficient chemiresistors owing to their continuous length, ensuring the direct signals transport between adjacent working electrodes for further enhanced gas sensing performances [11–18]. However, most of the metal oxides based chemiresistors still suffer from the poor selectivity owing to those metal oxides can react with several gases simultaneously. Thus construction of high-efficient metal oxides based chemiresistors with good selectivity is highly desirable in future.

Ethanol, as the most common aliphatic alcohol, has been widely investigated in gas sensing field for its diverse and practical applications in biomedicine, hospital, wine industry, breathalyzers, traffic safety, laboratories, etc. [19–23]. Meanwhile, ethanol can also cause healthy issues, such as skin/eyes irritation, central nervous system depression, and acidosis [24]. During the environmental ethanol monitoring, a practical bottleneck lies in the cross-sensitivity between ethanol and acetone is very similar [25–28]. Therefore, a selective ethanol sensor to effectively discriminate ethanol from acetone and some other reducing gases is very useful for future science. Among various materials, $SnO_2$ has been considered as a key semiconductor material due to its excellent chemical and electrical properties [29]. $SnO_2$ is also the most widely studied material among all the oxides used for gas sensor applications [30]. Herein, we demonstrate a rapid, sensitive, and selective ethanol sensor based on $Sr^{2+}$-doped $SnO_2$ nanofibers through electrospinning and calcination. After Sr-doping, the sensitivity against 100 ppm ethanol has been enhanced from ~10.8 to ~18.9. On the contrary, the sensitivity against 100 ppm acetone has been weaken from ~8.9 to ~3.9, resulting in good discriminative ability to ethanol from acetone. Furthermore, the sensor also displays good selectivity.

* Corresponding authors at: Alan G. MacDiarmid Institute, Jilin University, Changchun 130012, PR China. Fax: +86 431 85168292.
*E-mail addresses:* zhenyu_li@jlu.edu.cn (Z. Li), cwang@jlu.edu.cn (C. Wang).

http://dx.doi.org/10.1016/j.jcis.2014.09.056
0021-9797/

## 2. Materials and methods

### 2.1. Chemical

Ethanol (>95%), N,N-dimethyl formamide (>95%) and $SnCl_2{\cdot}2H_2O$ were obtained from Tianjin Chemical Co. (China). $Sr(NO_3)_2$ was purchased from Beijing Chemical Co. (China). Poly (vinyl pyrrolidone) (PVP, Mw = 1,300,000) was obtained from Aldrich. All chemicals were used as received without any further purification.

### 2.2. Preparation of Sr-doping $SnO_2$ nanofibers

In a typical procedure, 0.4 g of $SnCl_2{\cdot}2H_2O$ was dissolved in a mixture of DMF (4.4 g) and ethanol (4.4 g) under vigorous stirring for 10 min. Subsequently, 0.8 g PVP and a certain amount of $Sr(NO_3)_2$ were added into the above solution under vigorous stirring for 30 min. The obtained mixture was loaded into a glass syringe with a needle of 1 mm in diameter at the tip and electrified using a high-voltage DC supply. 15 kV was provided between the tip of the spinning nozzle and the collector at a distance of 20 cm. Finally, the fibers were peeled off from the collector and placed in a crucible. Calcination was performed at 600 °C in air for 5 h to remove the organic constituents of PVP and crystallize the $SnO_2$. The as-prepared nanofibers with different Sr doping levels of 1 at.%, 2 at.%, 3 at.% and 4 at.% were prepared according to the above methods.

### 2.3. Fabrication and measurement of gas sensor

The fibers were mixed with deionized water in a weight ratio of 100:15 and were ground to form a dilute paste. The paste was spin-coated onto a ceramic tube on which a pair of gold electrodes was previously printed, and then a Pt heating wire was inserted into the tube to form a side-heated gas sensor. The sensors were dried for 2 days before the first measurement.

The sensing properties were measured using a dynamic flow system, in which the resistance changes of the fibers were measured upon exposure to various levels of target molecules' vapors. Experimentally, the target molecules' vapors were injected into a sealed glass test chamber (20 L in volume) by a syringe through a rubber plug. After fully mixed with air (Relative Humidity (RH) was about 20%), the sensor was put into the test chamber. When the response reached a constant value, the sensor was exposed in air to recover. The electrical properties of the sensor were measured by the CGS-8 intelligent test system (Beijing Elite Tech Co. Ltd., China). This multichannel system consists of heating system, gas distribution system, measurement and data acquisition system, and measurement control software, which is ideally suited for comparative analysis of sensor performance in the same environmental conditions. The sensor response was measured between 220 and 380 °C, which is defined as the ratio $R_a/R_g$, where $R_a$ is the resistance in air, and $R_g$ is the resistance in test gas [31]. The time taken by the sensor to achieve 90% of the total resistance change is defined as the response time in the case

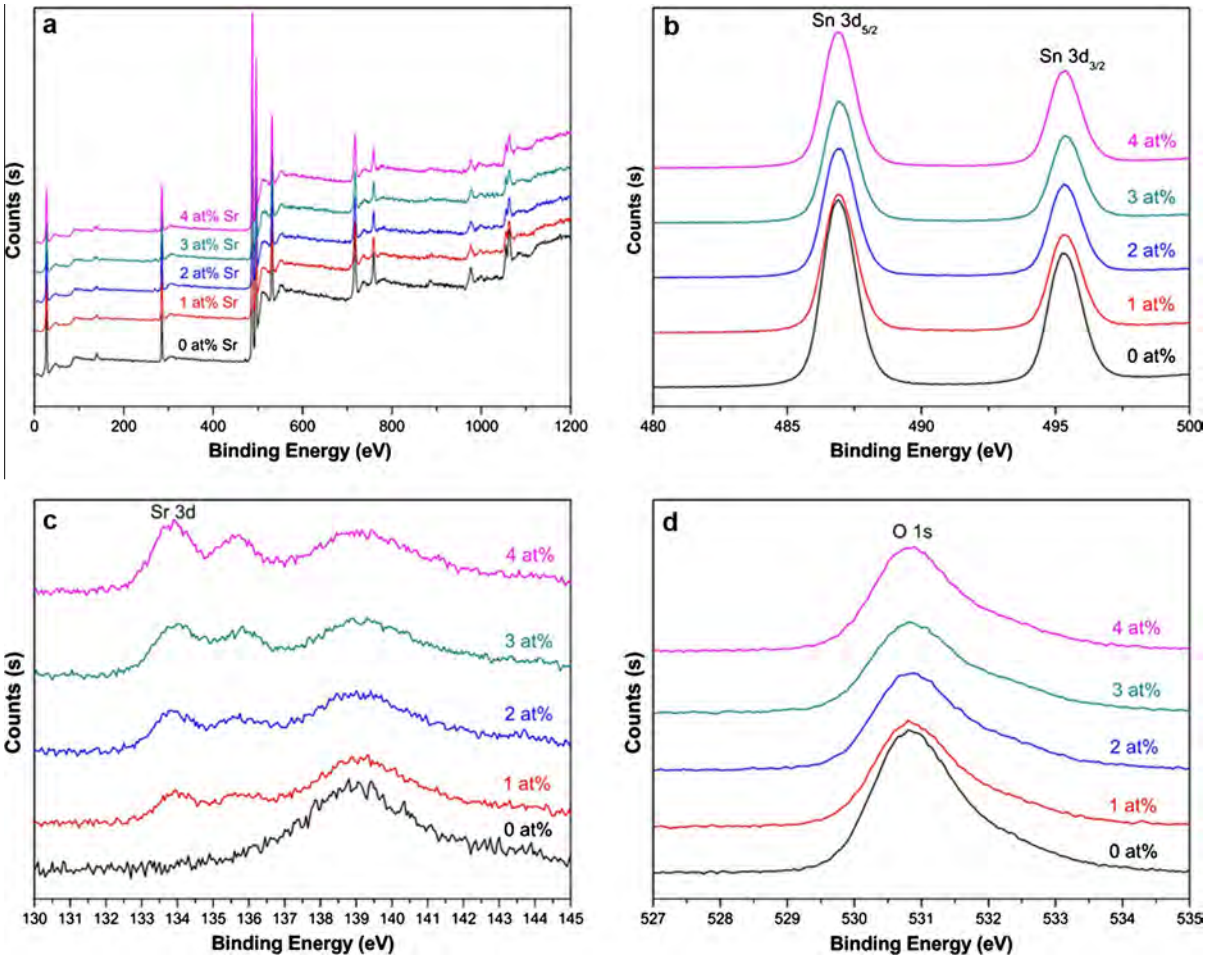


**Fig. 1.** XPS spectra of the Sr-doped $SnO_2$ with different $Sr^{2+}$ doping levels, (a) the survey XPS spectra, (b) Sn3d, (c) Sr3d, and (d) O1s.

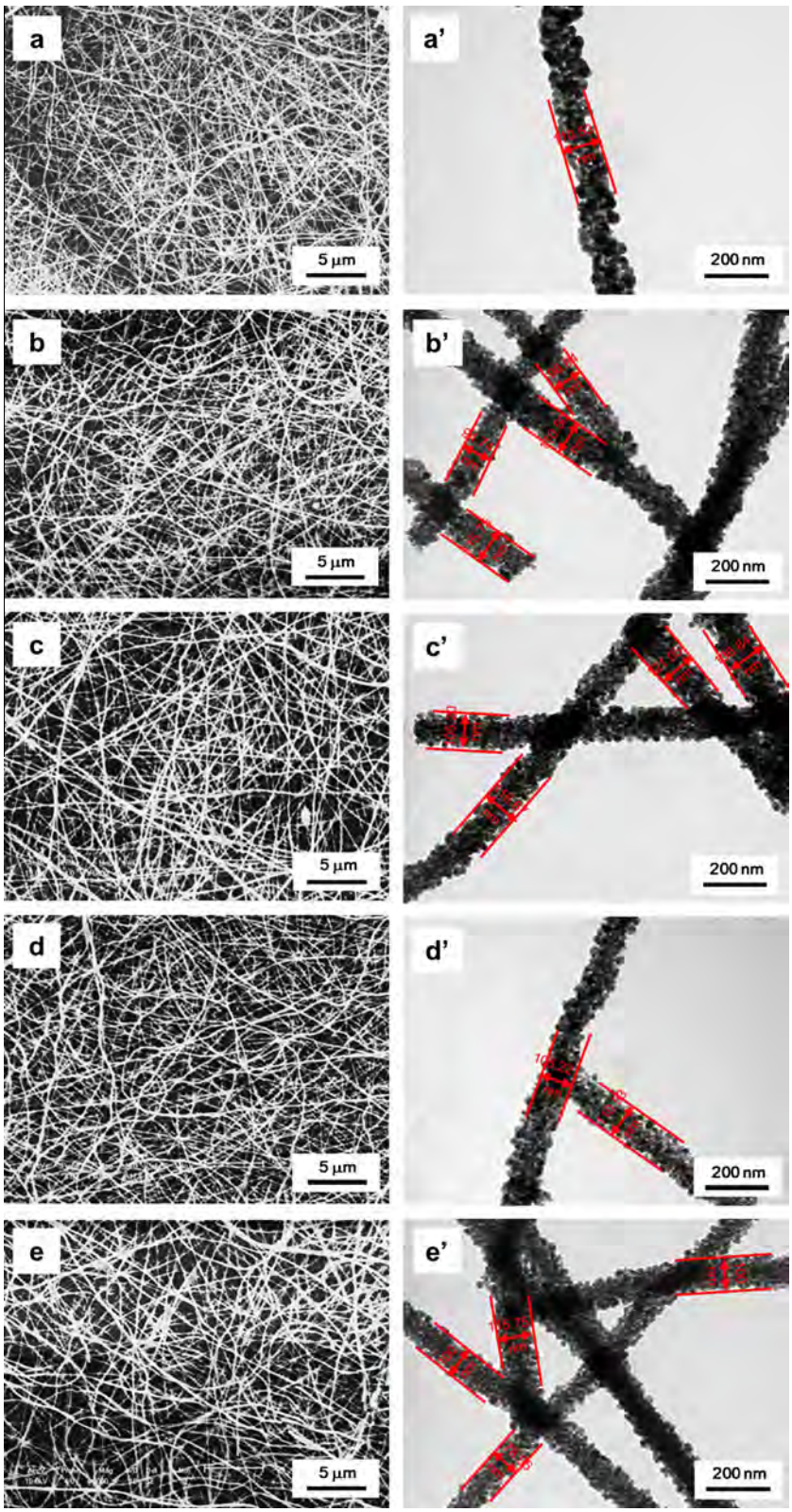


**Fig. 2.** SEM and TEM images of $Sr^{2+}/SnO_2$ nanofibers. The Sr doping concentration of (a) and (a′), (b) and b′), (c) and (c′), (d) and (d′), (e) and (e′) is 0 at.%, 1 at.%, 2 at.%, 3 at.%, and 4 at.%, respectively.

of adsorption or the recovery time for desorption. This testing method has been developed by Wang et al. [32]. All these measurements were taken when the mixed gas system reached its balance.

### 2.4. Characterization

The nanofibers were characterized by Transmission electron microscopy (TEM, Hitachi S-570) and X-ray photoelectron spectra

(XPS, ESCLAB MKII using Al as the exciting source). Crystal structures were measured by X-ray diffraction (XRD, Empyrean, PANalytical B.V. with a Cu Kα radiation).

## 3. Results and discussion

### 3.1. Structural and morphological characteristics

The surface composition and chemical state of the elements existing in Sr-doped $SnO_2$ nanofibers have been systematically characterized by XPS and shown in Fig. 1. Fig. 1a shows the survey XPS spectra of the final products. All the binding energies at various peaks were calibrated according to C element (the binding energy of C 1s plane is 284.6 eV). The spin–orbit components ($3d_{3/2}$ and $3d_{5/2}$) of the Sn 3d peak were both observed at 495.5 and 487.1 eV as shown in Fig. 1b, corresponding to $Sn^{4+}$ in a tetragonal rutile structure [33]. The $Sr3d_{3/2}$ peak and $Sr3d_{5/2}$ peak were detected at 135.5 eV and 133.7 eV, confirming that the chemical state of Sr ions in the fibers is $Sr^{2+}$ as shown in Fig. 1c [34,35]. Fig. 1d shows the O 1s core level spectra. The surface composition of Sr-doped $SnO_2$ nanofibers with different Sr doping levels have been calculated and provided in Table S1 in Supplementary Information.

Typical morphologies of $Sr^{2+}/SnO_2$ nanofibers with different Sr doping levels have been characterized by SEM. As shown in Fig. 2, all the $Sr^{2+}/SnO_2$ fibers maintain fibrous structures after the calcination and many nano-scaled pores are observed throughout the whole fiber films. TEM shows the average diameter of all the doped fibers is 110 ± 10 nm and nano-scaled pores within the nanofibers between the adjacent nanograins can be also observed. These micro/nano-scaled pores facilitate the absorption of target molecules in the final products, which favors the gas sensing performances [36].

The effects of Sr doping on $SnO_2$ crystal structures have been characterized by XRD as shown in Fig. 3a. All the strong diffraction peaks can be perfectly indexed as the tetragonal rutile structure of $SnO_2$ (JCPDS 41-1445) [37] and no diffraction peaks of strontium oxide phases were detected within the instrumental sensitivity. From the high-resolution of (1 1 0) peak (Fig. 3b), it can be clearly seen that the peaks of $Sr/SnO_2$ become broaden compared with pristine $SnO_2$, proving $Sr^{2+}$ doping can effectively inhibit the growth of $SnO_2$ gains during the calcination. Additionally, (1 1 0) peak shifts to a low angle when the Sr doping is 1 at.%, which indicates that $Sr^{2+}$ ions have been incorporated into $SnO_2$ lattice and occupy the tetragonal $Sn^{4+}$ cation sites of rutile $SnO_2$, forming $Sn_{\sim 0.99}Sr_{\sim 0.01}O_2$ metastable solid solution nanofibers. With further increasing the Sr doping levels, the (1 1 0) peak recovers a little, indicating that some Sr ions cannot be contained within the $SnO_2$ crystal and are expelled out the crystal, forming $SrO/SnO_2$ heterojunction nanofibers. Moreover, it is also suggested that no long ordering of SrO lattice is formed in the final composite nanofibers since no SrO peaks were detected. The formation of $Sn_{\sim 0.99}Sr_{\sim 0.01}O_2$

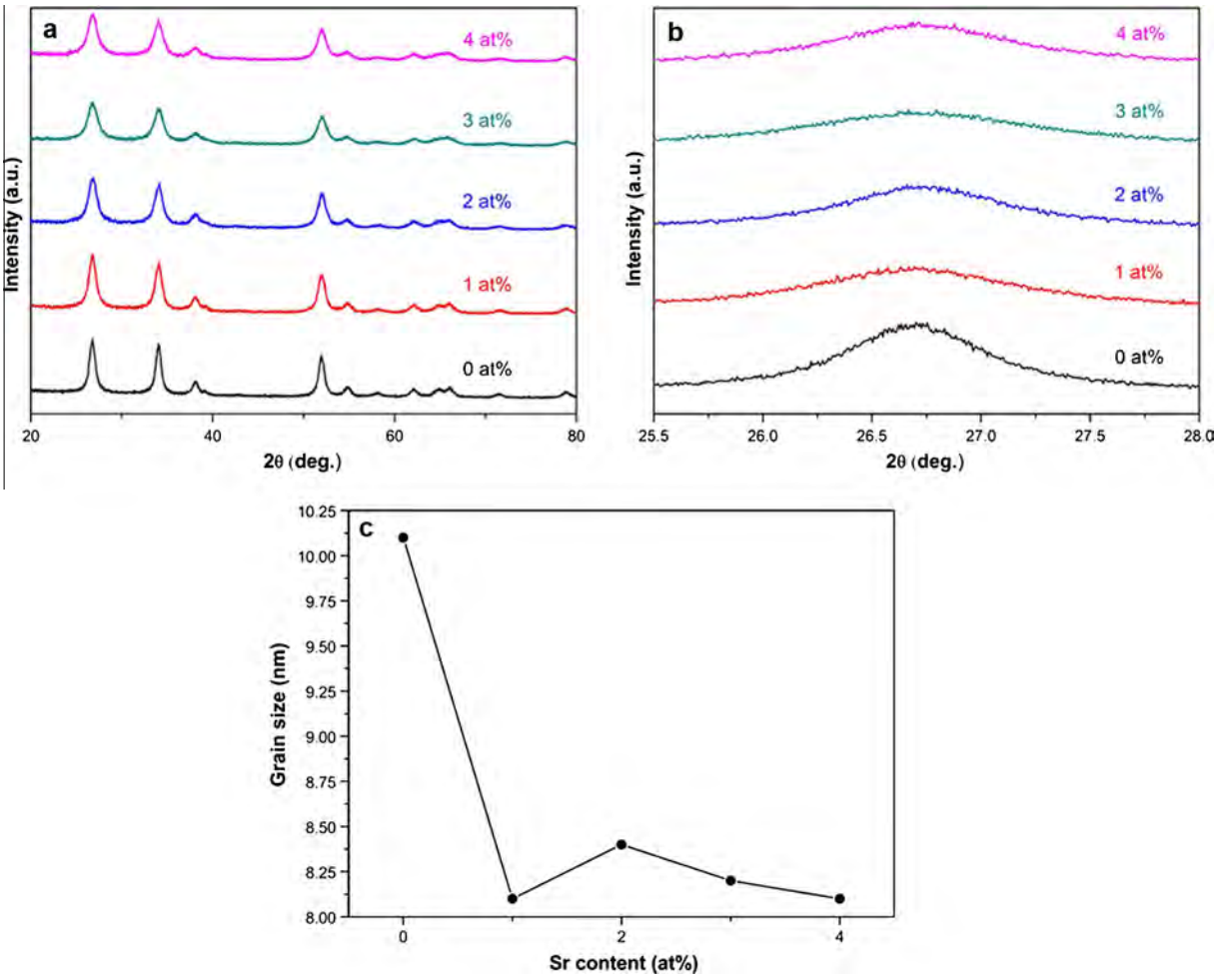


**Fig. 3.** (a) Full angel range of XRD patterns and (b) high-resolution of (1 1 0) peak of pristine and Sr-doped $SnO_2$ nanofibers with different doping levels; (c) grain sizes of $SnO_2$ as a function of Sr doping levels.

metastable solid solution nanofibers can be also supported by calculating the crystallite size of $SnO_2$ from the (110) peak via the Scherrer equation ($D = K\lambda/\beta\cos\theta$) [38]. The average crystalline size of $SnO_2$ is 10.1 nm for pristine $SnO_2$, 8.1 nm for 1 at.% Sr-doped $SnO_2$ nanofibres, 8.4 nm for 2 at.% Sr-doping, 8.2 nm for 3 at.% Sr-doping, and 8.1 nm for 4 at.% Sr-doping (Fig. 3c). The smallest crystal size of 1 at.% Sr-doped $SnO_2$ nanofibres implies the formation of $Sn_{\sim 0.99}Sr_{\sim 0.01}O_2$ metastable solid solution nanofibers.

### 3.2. Sensing performances

The optimal operating temperature of Sr-doped $SnO_2$ against 100 ppm of ethanol was confined by carrying out the tests at different temperatures as shown in Fig. 4a.

Volcano-shaped curves were obtained with the peak at 260 °C for all the samples, which indicates that optimal operating temperature of all samples is 260 °C and Sr-doping does not change the optimal operating temperature. Fig. 4b shows the response versus ethanol concentration (10–5000 ppm) at 260 °C with different Sr doping levels. As shown in Fig. 4b, Sr doping greatly improves the sensing response to ethanol. The responses increase continuously with the increase of ethanol concentration. The sensors do not saturate even when the concentration of ethanol reaches 5000 ppm. Among all the samples, $Sn_{\sim 0.99}Sr_{\sim 0.01}O_2$ metastable solid solution nanofibers display the highest sensing response (~19). Thus, $Sn_{\sim 0.99}Sr_{\sim 0.01}O_2$ metastable solid solution nanofibers and pristine $SnO_2$ are chosen for the following measurements.

Response/recovery behavior is an important factor to evaluate whether sensor can rapidly monitor the target molecules in time. The response/recovery behavior of $Sr^{2+}$-doped $SnO_2$ nanofibers was also studied against 100 ppm ethanol at 260 °C as shown in Fig. 5. For pristine $SnO_2$ nanofibers, the response and recovery behavior is 2s and 11s, respectively. For $Sn_{\sim 0.99}Sr_{\sim 0.01}O_2$ metastable solid solution nanofibers, response time does not change but recovery time has been shortened to 8s, indicating the Sr-doping can effectively enhance the desorption rate of ethanol on the surface.

To better understand the effect of dimensionalities on the gas sensing performances, zero-dimensional (0D) $SnO_2$ and $Sr^{2+}$-doped $SnO_2$ nanoparticles have been fabricated and characterized (Fig. S1 and S2 in Supplementary Information). Their gas sensing performances have been also tested (Fig. S3 in Supplementary Information). From the data, we can found that sensing performances of 1D nanofibers are higher than those of 0D nanoparticles. Additionally, we also prove the generality on such enhanced

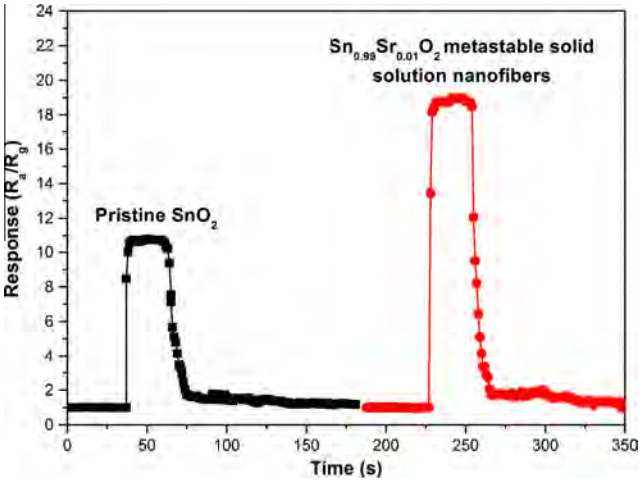


**Fig. 5.** Response and recovery behaviors based on pristine and $Sn_{\sim 0.99}Sr_{\sim 0.01}O_2$ metastable solid solution nanofibers against 100 ppm ethanol at 260 °C.

sensing performances caused by Sr doping by measuring the responses against over branched alcohols (Fig. S4 in Supplementary Information).

The enhanced ethanol sensing performances of Sr-doped $SnO_2$ nanofibers can be explained from two aspects: (i) When Sr was introduced into $SnO_2$ nanofibers, the mismatch ions diameters between $Sn^{4+}$ (69 pm) and $Sr^{2+}$(112 pm) inhibit the growth of $SnO_2$ grains (Fig. 3c), which can provide more active sites throughout the Sr–$SnO_2$ metastable solid solution nanofibers and the small crystal sized of the Sr–$SnO_2$ enlarge the surface area, leading to enhanced sensing performances. As the Sr doping concentration increased to be higher than 2 at.%, the enhanced sensing mechanism lies in the p–n heterojunction effect [39,40]. In an oxidizing atmosphere, a thicker charge depletion layer can be formed near the grain surface of $SnO_2$, giving rise to increased resistance. As exposing to the reducing target molecules, the number of electrons in the $SnO_2$ increases and the concentration of holes in SrO decreases. In other words, the thinner depletion layer thickness results in lower resistance. The thicker depletion layer in the oxidizing atmosphere and the thinner depletion thickness in the reducing atmosphere leads to the enhanced sensing performances. (ii) It has been proven that ethanol gas undergoes dehydrogenation on the basic properties of the oxide catalyst [41], namely, $C_2H_5OH \rightarrow CH_3CHO + H_2$ (basic oxide). When SrO, a typical basic metal oxide, was introduced into the $SnO_2$ system, basic surface on the

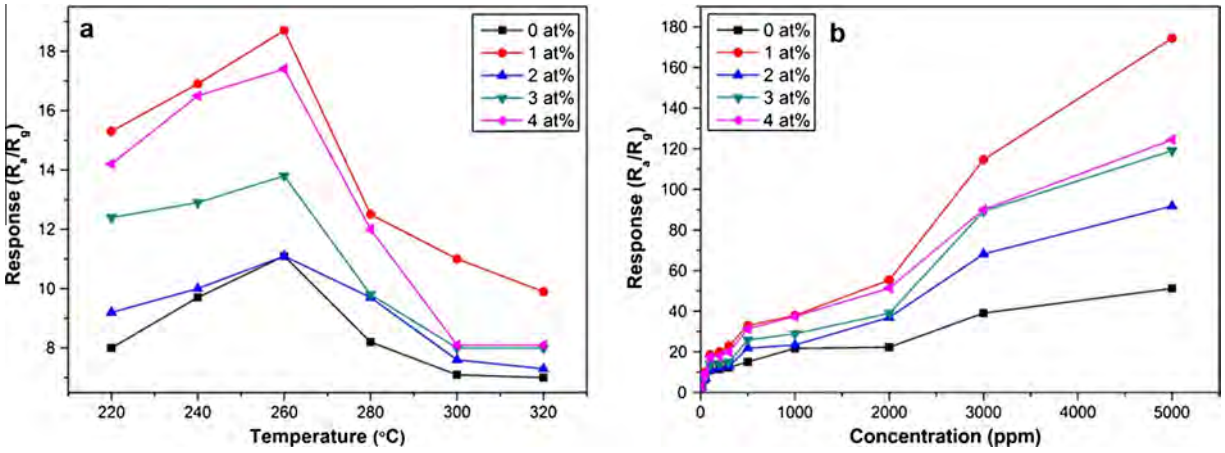


**Fig. 4.** (a) Responses of Sr-doped $SnO_2$ composite nanofibers against 100 ppm ethanol as a function of operating temperature and (b) linear plots of the responses of Sr-doped $SnO_2$ sensors against ethanol concentration at 260 °C.

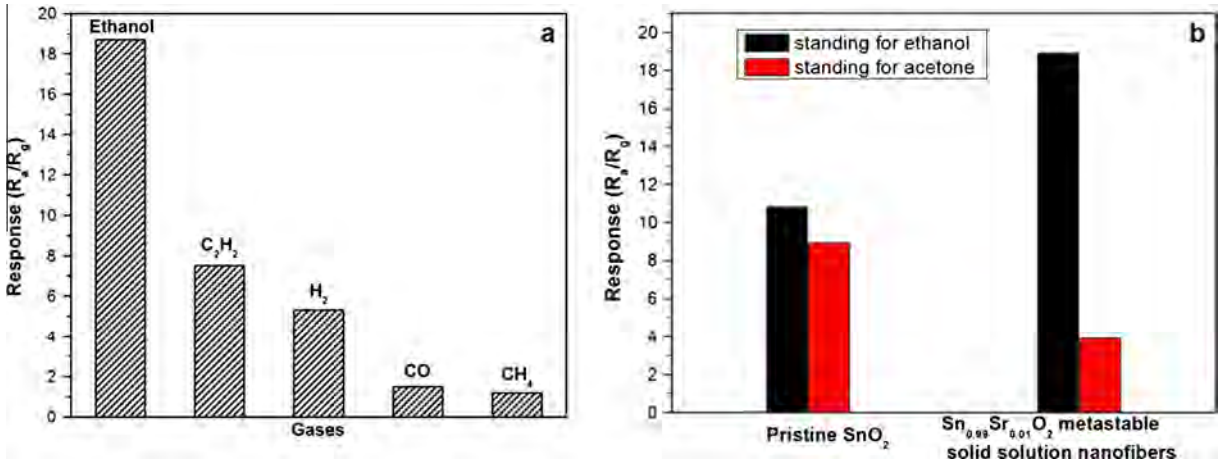


**Fig. 6.** (a) Cross-sensitivities of the sensor to ethanol, carbon monoxide, methane, acetylene, and hydrogen and (b) discriminative ability to ethanol from acetone after Sr-doping.

$SnO_2$ can be constructed. As proven by Yamazoe and co-workers, the basic surface can not only enhance the catalytic activity for the dehydrogenation of ethanol gas to $CH_3CHO$, but also show strong ability for the consecutive oxidation of $CH_3CHO$ to $CO_2$ [41], resulting in enhanced ethanol sensitivity.

The cross-selectivity of the sensor based on $Sn_{\sim 0.99}Sr_{\sim 0.01}O_2$ metastable solid solution nanofibers was investigated by measuring the response of sensor against some typical reducing gases including carbon monoxide, methane, acetylene, and hydrogen (experiments were carried out at 260 °C with gaseous concentration of 100 ppm). It can be clearly observed that $Sn_{\sim 0.99}Sr_{\sim 0.01}O_2$ metastable solid solution nanofibers showed high selectivity towards ethanol among all the gases as shown in Fig. 6a. It is been reported that the cross-sensitivity between ethanol and acetone is very similar [25–28], so good discriminative ability to ethanol from acetone is very important for ethanol sensors in practice. Fig. 6b shows the discriminative ability to ethanol from acetone based on pristine $SnO_2$ nanofibers and $Sn_{\sim 0.99}Sr_{\sim 0.01}O_2$ metastable solid solution nanofibers. For pristine $SnO_2$ nanofibers, the response to ethanol and acetone is ~10.8 and ~8.9 at 260 °C, respectively. Interestingly, the response to ethanol and acetone is 18.9 and 3.9 at 260 °C based on $Sn_{\sim 0.99}Sr_{\sim 0.01}O_2$ metastable solid solution nanofibers. Thus, the good discriminative ability to ethanol from acetone has been realized, which can be derived from two aspects: (i) Sr doping can effectively lower the adsorption rate of acetone on the surface of $Sn_{\sim 0.99}Sr_{\sim 0.01}O_2$ metastable solid solution nanofibers; (ii) different responses on the dehydrogenation products of ethanol and acetone, namely, $CH_3CHO$, $H_2$, and CO ($CH_3COCH_3 \rightarrow CH_3CHO + CO$) [42]. $CH_3CHO$ appears within the dehydrogenation products of both ethanol and acetone, thus the effect of $CH_3CHO$ can be neglected. As illustrated in Fig. 6a, the responses of $H_2$ is ~5.3, whereas the response of CO is much weaker (~1.5), resulting in the weak response of acetone. Those two aspects lead to the good discriminative ability to ethanol from acetone.

## 4. Conclusions

In summary, a new rapid, sensitive, and selective ethanol sensor has been demonstrated based on $SnO_2$ nanofibers enabled by basic Sr-doping. The as-prepared sensor exhibits high response value (~18.9) to ethanol at 260 °C with the response/recovery of 2s/8s, respectively. Interestingly, the basic Sr-doping could not only enhance the ethanol sensitivity but also weaken the acetone sensitivity, thus good discriminative ability ethanol from acetone can be realized. These superior performances make our samples promising candidates in development and realization of a low-cost and high-performance ethanol sensor in future.

## Acknowledgments

The work has been supported by National 973 Project (Nos. 2007CB936203 and S2009061009) and NSF China (No. 51003036).

## Appendix A. Supplementary material

Supplementary data associated with this article can be found, in the online version, at http://dx.doi.org/10.1016/j.jcis.2014.09.056.

## References

[1] S. Ehrmann, J. Jüngst, J. Goschnick, D. Everhard, Sens. Actuators B: Chem. 65 (2000) 247–249.
[2] A.A. Tomchenko, G.P. Harmer, B.T. Marquis, Sens. Actuators B: Chem. 108 (2005) 41–55.
[3] S. Zampolli, I. Elmi, J. Stürmann, S. Nicoletti, L. Dori, G.C. Cardinali, Sens. and Actuators B: Chem. 105 (2005) 400–406.
[4] N. Ramgir, N. Datta, M. Kaur, S. Kailasaganapathi, A.K. Debnath, D.K. Aswal, S.K. Gupta, Colloids Surf. A: Physicochem. Eng. Aspects 439 (2013) 101–116.
[5] A. Kolmakov, M. Moskovits, Annu. Rev. Mater. Res. 34 (2004) 151–180.
[6] D.H. Zhang, Z.Q. Liu, C. Li, T. Tang, X.L. Liu, S. Han, B. Lei, C.W. Zhou, Nano Lett. 4 (2004) 1919–1924.
[7] M. Batzill, U. Diebold, Progr. Surf. Sci. 79 (2005) 47–154.
[8] A. Kolmakov, D.O. Klenov, Y. Lilach, S. Stemmer, M. Moskovits, Nano Lett. 5 (2005) 667–673.
[9] E. Comini, Anal. Chim. Acta 568 (2006) 28–40.
[10] R. Bajpai, A. Motayed, A.V. Davydov, V.P. Oleshko, G.S. Aluri, K.A. Bertness, M.V. Rao, M.E. Zaghloul, Sens. Actuators B – Chem. 171–172 (2012) 499–507.
[11] Z.Y. Li, H.N. Zhang, W. Zheng, W. Wang, H.M. Huang, C. Wang, et al., Highly sensitive and stable humidity nanosensors based on LiCl doped $TiO_2$ electrospun nanofibers, J. Am. Chem. Soc. 130 (2008). 5036-+.
[12] Q. Qi, T. Zhang, L. Liu, X.J. Zheng, Sens. Actuators B – Chem. 137 (2009) 471–475.
[13] X.F. Song, Z.J. Wang, Y.B. Liu, C. Wang, L.J. Li, Nanotechnology 20 (2009).
[14] W. Zheng, X.F. Lu, W. Wang, Z.Y. Li, H.N. Zhang, Y. Wang, Z.J. Wang, C. Wang, Sens. Actuators B – Chem. 142 (2009) 61–65.
[15] W.S. Kim, B.S. Lee, D.H. Kim, H.C. Kim, W.R. Yu, S.H. Hong, Nanotechnology 21 (2010).
[16] L. Liu, C.C. Guo, S.C. Li, L.Y. Wang, Q.Y. Dong, W. Li, Sens. Actuators B – Chem. 150 (2010) 806–810.
[17] J. Moon, J.A. Park, S.J. Lee, T. Zyung, I.D. Kim, Sens. Actuators B – Chem. 149 (2010) 301–305.
[18] M.M. Arafat, B. Dinan, S.A. Akbar, A. Haseeb, Sensors 12 (2012) 7207–7258.
[19] E.T. Hayes, A. Galal, H.B. Mark Jr, Talanta 42 (1995) 873–877.
[20] J.K. Park, H.J. Yee, S.T. Kim, Biosens. Bioelectron. 10 (1995) 587–594.
[21] C.X. Cai, K.H. Xue, Y.M. Zhou, H. Yang, Talanta 44 (1997) 339–347.
[22] T. Qin, X. Xu, T. Polák, V. Pacáková, K. Štulík, L. Jech, Talanta 44 (1997) 1683–1690.
[23] B. Kieser, F. Dieterle, G. Gauglitz, Anal. Chem. 74 (2002) 4781–4787.

[24] A. Umar, F. Al-Hazmi, G.N. Dar, S.A. Zaidi, R.M. Al-Tuwirqi, F. Alnowaiserb, A.A. Al-Ghamdi, S.W. Hwang, Sens. Actuators B: Chem. 166–167 (2012) 97–102.
[25] B.L. Zhu, C.S. Xie, W.Y. Wang, K.J. Huang, J.H. Hu, Mater. Lett. 58 (2004) 624–629.
[26] H. Gong, Y.J. Wang, S.C. Teo, L. Huang, Sens. Actuators B: Chem. 54 (1999) 232–235.
[27] Z. Jing, S. Wu, Mater. Lett. 60 (2006) 952–956.
[28] J. Zhao, L.H. Huo, S. Gao, H. Zhao, J.G. Zhao, Sens. Actuators B: Chem. 115 (2006) 460–464.
[29] M.Y. Wu, W. Zeng, Y.Q. Li, Mater. Lett. 104 (2013) 34–36.
[30] K.J. Choi, H.W. Jang, Sensors 10 (2010) 4083–4099.
[31] P. Feng, X.Y. Xue, Y.G. Liu, T.H. Wang, Appl. Phys. Lett. 89 (2006) 243514.
[32] Y.X. Liang, Y.J. Chen, T.H. Wang, Appl. Phys. Lett. 85 (2004) 666–668.
[33] H.J. Ahn, H.C. Choi, K.W. Park, S.B. Kim, Y.E. Sung, J. Phys. Chem. B 108 (2004) 9815–9820.
[34] T. Shahwan, H.N. Erten, Radiochim. Acta 93 (2005) 225–232.
[35] L. Qiao, T.C. Droubay, V. Shutthanandan, Z. Zhu, P.V. Sushko, S.A. Chambers, J. Phys. – Condens. Matter 22 (2010).
[36] G. Sakai, N. Matsunaga, K. Shimanoe, N. Yamazoe, Sens. Actuators B: Chem. 80 (2001) 125–131.
[37] B. Cheng, J.M. Russell, J. Am. Chem. Soc. 126 (2004) 5972–5973.
[38] R.A. Young, A. Sakthivel, T.S. Moss, C.O. Paiva-Santos, J. Appl. Crystallogr. 28 (1995) 366–367.
[39] J.H. Yu, G.M. Choi, Sens. Actuators B: Chem. 75 (2001) 56–61.
[40] Z.J. Wang, Z.Y. Li, H.N. Zhang, W. Wang, C. Wang, J. Phys. Chem. C 114 (2010) 6100–6105.
[41] T. Jinkawa, G. Sakai, J. Tamaki, N. Miura, N. Yamazoe, J. Mol. Catal. A: Chem. 155 (2000) 193–200.
[42] X. Chi, C.B. Liu, L. Liu, Y. Li, Z.J. Wang, X.Q. Bo, L.L. Liu, C. Su, Sens. Actuators B: Chem. 194 (2014) 33–37.